Determination of the beam asymmetry Σ in η- and η'-photoproduction using Bayesian statistics

Jakob Michael Krause

Masterarbeit in Physik
angefertigt im Helmholtz-Institut für Strahlen- und Kernphysik

vorgelegt der
Mathematisch-Naturwissenschaftlichen Fakultät
der
Rheinischen Friedrich-Wilhelms-Universität
Bonn

Sep 2022

I hereby declare that this thesis was formulated by myself and that no sources or tools other than those cited were used.

Bonn, ... Date .... Signature

1. Gutachterin: Jun. Prof. Dr. Annika Thiel
2. Gutachter: Prof. Dr. Jochen Dingfelder

Contents

CHAPTER 2

Experimental Setup

In this work the beam asymmetry Σ is determined in the reactions $\gamma p \to p\eta$ and $\gamma p \to p\eta'$, requiring a polarized photon beam and an unpolarized proton target. It is convenient to study photoproduction off a fixed target and investigate the resonances that occur in the process. The analyzed data was taken at the CBELSA/TAPS experiment located in Bonn at the ELectron Stretcher Accelerator (ELSA). In this chapter the different parts of the CBELSA/TAPS experiment that are used for the measurement of the beam asymmetry Σ will be presented. Figure 2.1 shows an overview of the experimental hall. All mentioned parts are discussed in detail in the following High energy electrons extracted from ELSA

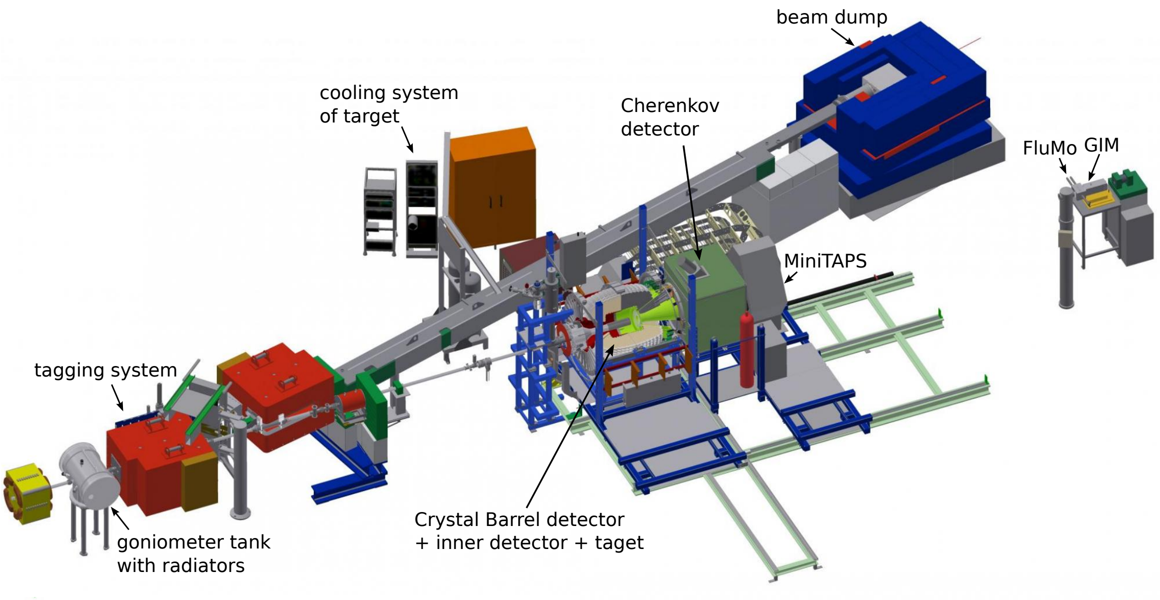

Figure 2.1: Overview of the experimental hall of the CBELSA/TAPS experiment. The electron beam from ELSA enters at the top right. M. GRÜNER in [Afz19]

are used to produce a polarized photon beam using the *bremsstrahlung* process (see 2.1.1). After they have been energy tagged (see 2.1.2) these photons then interact with the fixed target material (see Section 2.2) so that hadronic resonances may be excited that will decay via the strong interaction under the emission of mesons. The resulting decay products can then be measured with a system of electromagnetic calorimeters and scintillators that is especially suited for the detection of photons (see Section 2.3). The analogue measurements are only saved for offline analysis if detector signals meet certain trigger conditions which is only the case for reactions that are of interest (see Section 2.4). This way the amount of unwanted background is minimized already during the process of data taking. Once data acquisition is finished the data may be investigated with the help of analysis software and Monte Carlo simulations tailored to the needs of the CBELSA/TAPS experiment (see Section 2.5).

2.1 Production of polarized high energy photon beam

To measure polarization observables in photoproduction reactions a polarized photon beam is needed which can be created using *coherent bremsstrahlung*. Bremsstrahlung is the dominating interaction of high energy ($\mathcal{O}$ (1 GeV)) electrons with matter [Leo94]. Electrons are decelerated in the Coloumb field of heavy nuclei and radiate real photons, see Figure 2.2.

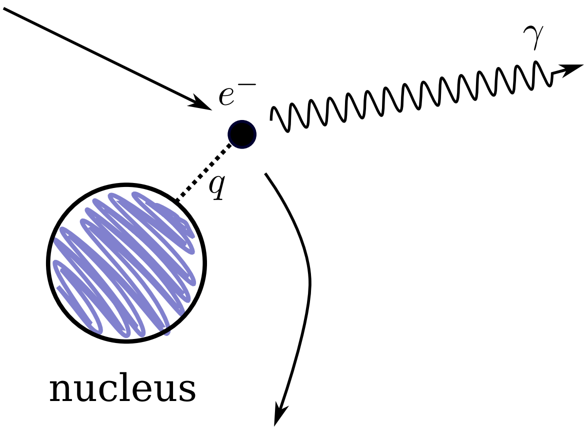

Figure 2.2: Illustration of the bremsstrahlung process: An electron e^- is deflected in the Coloumb field of a nucleus in the radiator material. A photon γ is emitted and so the momentum q is transferred.

To conserve momentum there has to be a momentum transfer q which is negligibly small compared to the nucleon mass. If an amorphous radiator is used incoherent bremsstrahlung is produced with a continuous spectral distribution proportional to $1/E_\gamma$ according to the Bethe-Heithler cross section [Hei54]. Since the structure of nuclei in the amorphous radiator does not exhibit any periodicity, the electric field vector will not prefer any particular direction, resulting in a net polarization degree of zero for the photon beam. To achieve non-vanishing polarization degrees a crystal with periodic placement of nuclei may be used as radiator. Then, coherent bremsstrahlung is produced; the crystal can absorb the recoil only for discrete momenta q_n meeting the Laue condition [Dem10] of the crystal lattice. This enables constructive interference between different bremsstrahl photons and at the same time fixes the deflection plane of incoming electrons, resulting in a coherent polarized photon beam. Incoherent bremsstrahlung may still occur due to impurities in the crystal structure, so that the total bremsstrahlung cross section off a crystal radiator σ_{crystal} is the sum of a coherent (σ_{coherent}) and an incoherent ($\sigma_{\text{incoherent}}$) part

$$\sigma_{\text{crystal}} = \sigma_{\text{coherent}} + \sigma_{\text{incoherent}}. \tag{2.1}$$

The process of bremsstrahlung can be modeled using ANalytical Bremsstrahlung (ANB) calculations [Nat+03]. ANB intensity spectra for a crystal and amorphous radiator are shown in Figure 2.3 on the left hand side. The right hand side shows the enhancement spectrum, which is given by dividing the two spectra. One observes that the bremsstrahlung intensity spectrum obtained from a crystal radiator

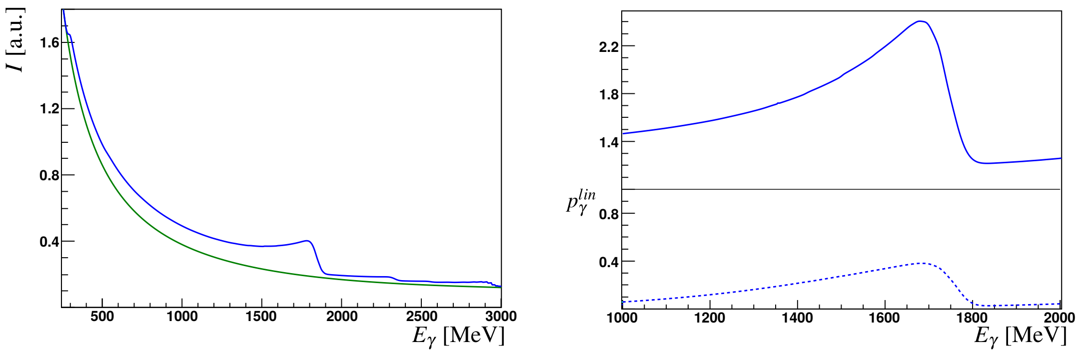

Figure 2.3: Left: Incoherent (green) and crystal (blue) bremsstrahlung intensities as a function of the photon energy. Right: The enhancement spectrum is given as the ratio of crystal to incoherent intensity spectrum. The dashed line at the bottom shows the calculated polarization degree. Both spectra are generated using ANB calculations. Taken from [Afz19].

is in general enhanced relative to the incoherent spectrum obtained from an amorphous radiator. In fact, using ANB calculations, the polarization degree can be determined from the enhancement spectrum. The characteristic drop in intensity in the intensity spectrum obtained from the crystal radiator is referred to as the coherent edge. It occurs because the photon energy in the kinematically allowed region of the recoil momentum that will lead to coherent bremsstrahlung is limited. The relative alignment of the radiation crystal to the electron beam determines the position of the coherent edge.

2.1.1 Goniometer

In order to determine the beam polarization from enhancement spectra, a diamond radiator as well as an amorphous radiator are required. Several radiators as well as beam diagnostics tools mounted inside a rotating aluminum wheel are part of the goniometer [Els+09], resting inside a vacuum tank. Depending on whether linearly polarized or unpolarized photons are needed either copper radiators of different thickness or a diamond radiator, which is located in the center of the wheel, are inserted into the beam axis, see Figure 2.4. In case a circularly polarized photon beam is required, a Møller polarimeter [Kam10] is used, which is also shown in Figure 2.4. The goniometer can be rotated in all directions allowing precise alignment with the incoming electron beam from ELSA.

2.1.2 Tagging system

Once the impinging electrons from ELSA have scattered off the radiator their energy is determined in order to measure the energy of the created photons. This is possible because the initial electron energy $E_0 = 3.2\,\text{GeV}$ is known from ELSA. Thus, the photon Energy E_γ is given by subtracting the energy of the recoil electrons E_e from E_0[1]

$$E_\gamma = E_0 - E_e. \tag{2.2}$$

The recoiling electrons are deflected towards the tagging system [For10] consisting of 96 overlapping scintillator bars and 480 scintillating fibers using the magnetic field of a dipole magnet with a field strength of 1.5 T. The bending radius of the electrons depends on their momenta is uniquely defined by the tagger hit position. With the position of the deflected electrons and the magnetic field strength, E_e can thus be determined. For an initial energy $E_0 = 3.2$ GeV the scintillator bars cover an energy range of $560\,\text{MeV} < E_\gamma < 3100\,\text{MeV}$ with an energy resolution of $0.1\%E_\gamma$-$6\%E_\gamma$. The fibers additionally improve the energy resolution in the energy range $416\,\text{MeV} < E_\gamma < 2670\,\text{MeV}$ to $0.1\%E_\gamma$-$0.4\%E_\gamma$. Photomultipliers are used for the readout of the tagger bars and fibers, realizing a time resolution of [2]$\text{FWHM}_\text{bar} = 635$ ps and $\text{FWHM}_\text{fiber} = 1.964$ ns [Har08]. Any electrons that have not interacted with the radiator material are deflected by another dipole magnet towards the beam dump, see Figure 2.1. Figure 2.5 shows a top-down view of the tagging system.

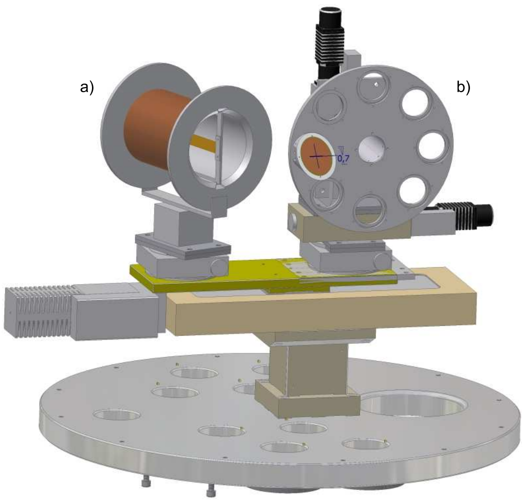

Figure 2.4: The goniometer holds several radiators that can be inserted onto the beam axis (b). Also available is a Møller radiator [Wal].

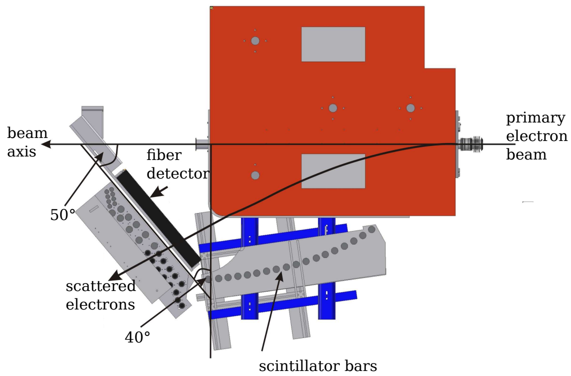

Figure 2.5: Top-down view of the tagging system consisting of dipole magnet (red) and scintillating bars and fibers [For10]. Electrons are deflected by the magnet after the bremsstrahlung process.

2.2 Liquid hydrogen target

The (polarized) photon beam impinges on a liquid hydrogen target [Ham09] which is located at the center of the crystal barrel detector, see Figure 2.1. It consists of a Kapton cell that measures 5.1 cm in length and 3 cm in diameter which is filled with liquid hydrogen. A separate cooling circuit with liquid hydrogen ensures the hydrogen that is used as target material stays liquid. Kapton is chosen as material for the target cell because the expected rate of hadronic reactions induced in the target cell is

[1] Hereby, the recoil energy absorbed by the nuclei is neglected.
[2] Full Width Half Maximum.

small compared to the expected rate from liquid hydrogen [Ham09]. Protons are bound with a binding energy of 21.4 eV in the target material, which is negligible on the scale of hadronic reaction energies, so that they can be considered free. A schematic view of the target is shown in Figure 2.6.

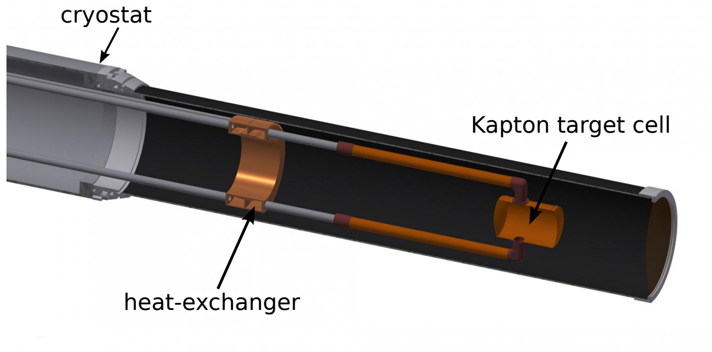

Figure 2.6: Schematic overview of the liquid hydrogen target. Two tubes connected to a heat exchanger and the Kapton cell allow filling it with liquid hydrogen. M. Grüner in [Afz19].

2.3 Detector system

Hadronic reactions are induced by the photon beam in the target material. As a consequence resonances are excited that decay under emission of mesons. These mesons subsequently decay to e.g. photons. The main calorimeters of the experiment, the Crystal Barrel that is complemented by the forward detector(2.3.2) and the MiniTAPS calorimeter (2.3.3), cover 95% of the solid angle 4π and are especially suited for the detection of photons. Charged particles are identified by the inner detector (2.3.1) as well as plastic scintillators mounted in front of the forward and the MiniTAPS detector that are used as vetoes. To suppress electromagnetic reactions a Čerenkov detector is used (2.3.4). The photon flux is measured via the Gamma-Intensity-Monitor (GIM) and Flux-Monitor (FluMo) (2.3.5).

2.3.1 Inner detector

The inner detector [Fös00; Suf+05] encloses the target in a cylindrical geometry and consists of 513 plastic scintillation fibers that are placed in three layers. The outer layer is oriented along the beam axis while the inner layers are tilted by an angle of $-24.5°$ and $25.8°$, respectively, see Figure 2.7. This structure allows to determine the azimuthal and polar angle of a charged particle as long as at least two layers are hit. The detector is in total 40 cm long and covers a polar angle range of $23.1° < \theta < 166°$ with a resolution of $0.4°$ in polar angle θ and $0.1°$ in azimuthal angle ϕ. The fibers consist of Polystyrene with a refractive index of $n = 1.6$ and are cladded by Polymethylmetacrylat ($C_5H_8O_2$) with $n = 1.49$ [PDG]. Charged particles passing the detector will cause the emission of scintillation light by the Polystyrene molecules which is read out with photomultipliers after passing lightguides. Short decay times ensure a fast time signal and a time resolution of FWHM = (2.093 ± 0.013) ns is reached [Har08].

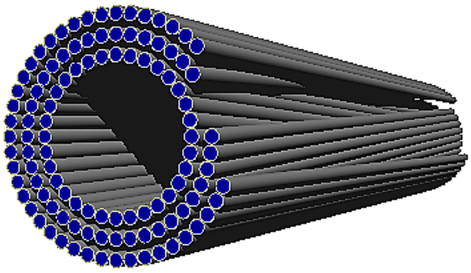

Figure 2.7: The inner detector with three layers of scintillating fibers. The inner two layers are tilted with respect to the outer layer. D. Walther in [Afz19].

2.3.2 Crystal Barrel and forward detector

The main calorimeter of the experiment is the Crystal Barrel detector [Ake+92]. It consists of 1320 CsI(Tl) crystals that are arranged in 24 rings facing the center of the target, see Figure 2.8. The first

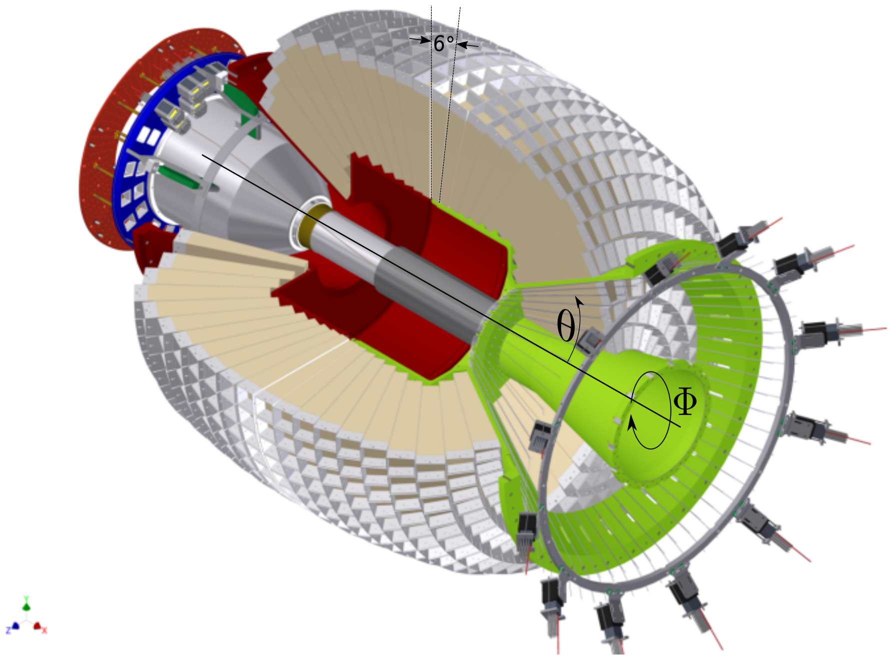

Figure 2.8: Crystal barrel calorimeter and forward detector are built such that they enclose the target and the inner detector. The forward detector consists of the first three rings (green base) of crystals which are additionally covered by plastic scintillators for charged particle identification. The definition of polar angle θ and azimuthal angle ϕ in the LAB system are indicated as well.D. Walther in [Urb17]

three rings in forward direction contain 30 crystals each and build the forward detector, covering the polar angle range $11.18° < \theta < 27.54°$. Also the 24^{th} ring contains 30 crystals, all other rings are made up of 60 crystals. The crystals are shaped like truncated trapezoidal pyramids that cover 6° in polar angle θ and azimuthal angle ϕ. Only in the first three and the last ring the crystals cover 12° in ϕ. Full coverage in ϕ and 80% ($12° < \theta < 156°$) coverage in θ are achieved by the forward detector and the Crystal Barrel. Photons from neutral mesonic decays are very high energetic and will interact with the inorganic scintillator material mainly via pair production [Leo94]. The produced electrons and positrons will themselves interact mainly via bremsstrahlung such that usually an electromagnetic shower is created upon photon impact that may spread over several crystals. Using crystals with a length of $l = 30\,\text{cm}$ photons with an energy of up to 2 GeV may deposit their entire energy in the calorimeter since the l corresponds to 16.22 radiation lengths X_0 [Ake+92]. The transversal spread of a shower is given by the Móliere radius which is 3.8 cm for CsI(Tl) [Ake+92]. By determining the focal point of the electromagnetic showers an angular resolution of less than 2° can be achieved [Jun04] while the energy resolution is given by [Ake+92]

$$\frac{\sigma_E}{E} = \frac{2.5\%}{\sqrt[4]{E/\text{GeV}}}, \tag{2.3}$$

depending on the initial photon energy E. The energy loss of heavier charged particles, e.g. a proton, is described by the Bethe-Bloch formula [Bet30]. Depending on their mass they only deposit their full energy up to a certain threshold energy above which they are characterized as Minimal Ionizing Particles (MIP).

The emitted scintillation light of crystals not belonging to the forward detector is read out using PIN photodiodes. A wavelength shifter ensures meeting the sensitive spectral range of the photodiodes. The long decay times of the scintillation light and the slow preamplifiers following the photodiodes do not allow the determination of a timing information for particles detected in the Crystal Barrel [3], so that the Crystal Barrel is optimized for energy measurements.

Crystals belonging to the forward detector are read out using Photomultipliers. They provide a faster signal, such that timing information for forward detector hits is available with a time resolution of FWHM = (1.861 ± 0.016) ns [Har08]. Additionally plastic scintillator plates are mounted in front [Wen04], allowing the identification of charged particles with an efficiency of 72% [Geh15]. Optical fibers guide the scintillation light from the plates to photomultipliers.

2.3.3 MiniTAPS

Since the Crystal Barrel only covers the solid angle starting at $\theta \approx 12°$. It is supplemented by the Mini-Two-Arm-Photon-Spectrometer (MiniTAPS) [Gab+94; Str96] for polar angles $1° < \theta < 12°$. The MiniTAPS detector is placed in a distance of $d = 2.1\,\text{m}$ from the target and consists of 216 hexagonally shaped BaF_2 crystals, see Figure 2.9. Each crystal has a length of $l = 25\,\text{cm}$ which is equivalent to 12 radiation lengths [Nov91] and a width of $w = 5.8\,\text{cm}$. The chosen material has a high density and is able to withstand high reaction rates [PDG]. This is important here because most reactions will be strongly boosted in forward direction towards small θ. Different mechanisms of scintillation allow to extract a fast and a slow component [Leo94] which are read out using photomultipliers and separately used for timing and energy information, respectively. Hereby a time

[3] As of 2014, the PIN photodiodes have been replaced by avalanche photodiodes (APD) [Hon14; Urb17], allowing a fast read out that can be used to provide timing information and also as part of the trigger.

resolution of FWHM = (0.872 ± 0.006) ns [Har08] and an energy resolution of [Gab+94]

$$\frac{\sigma_E}{E} = 1.9\% + 0.59\% \cdot \sqrt{E/\mathrm{GeV}} \tag{2.4}$$

is achieved. At the same time an angular precision of 0.2° in θ is reached.

In front of each BaF_2 crystal, plastic scintillator plates are mounted to identify charged particles. Their scintillation light is guided towards photomultipliers using optical fibers. With these scintillators a time resolution of FWHM = (3.06 ± 0.05) ns is obtained [Har08].

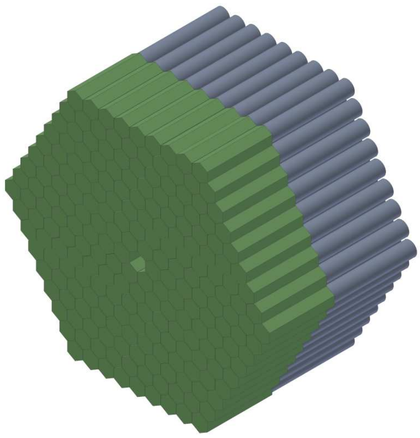

Figure 2.9: The MiniTAPS detector is made up of 216 BaF_2 crystals (grey). In front of each crystal, plastic scintillators are mounted for charged particle information. Taken from [Wal].

2.3.4 Čerenkov detector

When the photon beam impinges on the proton target, not only hadronic reactions are induced but also electromagnetic reactions. Because the beam energy is very high on the scale of electromagnetic interactions, any produced electrons and positrons are highly relativistic and boosted to small polar angles. To suppress these events already during data acquisition a Čerenkov detector [Kai07] is positioned between the MiniTAPS calorimeter and the Crystal Barrel, see Figure 2.1. It is filled with CO_2 gas where Čerenkov light is emitted by electrons or positrons above an energy of 17.4 MeV. This follows from the refractive index which is given as $n_{CO_2} = 1.00045$ [PDG]. The emitted Čerenkov radiation is focused on a photodiode using a parabolic mirror. The presence of a signal can then be used as veto during data acquisition to reduce the amount of recorded electromagnetic background. Electrons and positrons are detected with an efficiency of up to (99.72 ± 0.45)% [Kai07].

2.3.5 Flux monitoring

The FluMo and GIM detector are used to determine the total number of photons incident on the target and are located behind the MiniTAPS detector, as is shown in Figure 2.1.

The GIM detector [McG08] is made of 16 PbF_2 crystals placed in a 4×4 array, see Figure 2.10. Incoming photons will interact with the material mainly via pair production [Leo94]. The produced electrons and positrons are highly relativistic and will emit Čerenkov light that is collected with photomultipliers. For reaction rates higher than 5 MHz the GIM detector efficiency decreases significantly. For rates above 7 MHz more than 10% of events are not registered [Har08]. To

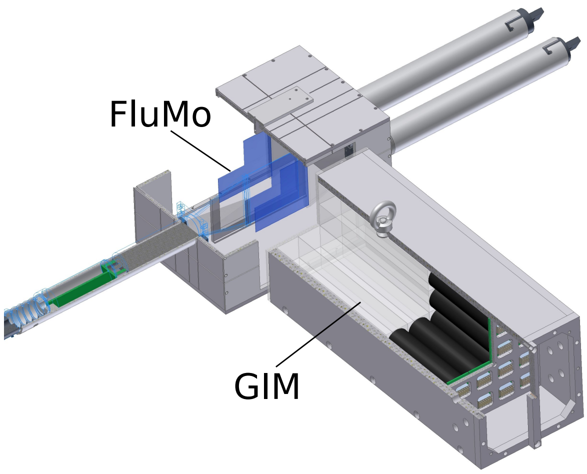

Figure 2.10: The two detectors FluMo and GIM are used to monitor the photon flux at different reaction rates. D. Walther in [Afz19].

compensate this the FluMo detector [Die08] is used as soon as deadtime effects influence the performance of the GIM detector. A converter plate made of lead, two scintillators and a veto detector are part of the FluMo detector. Impinging photons may create electron positron pairs that are detected in a coincidence measurement using the two scintillators. A plastic scintillation detector is placed before the converter plate and gives a veto signal if charged particles pass through it.

2.4 Trigger

To minimize the volume of data that is saved to disk for offline analysis, data is only digitized if certain predefined patterns in the detector signals are present. The search for predefined patterns is managed by the trigger of the experiment. The analyzed data sets were acquired using the *vme_trig42c* trigger [Win06; Hof18]. The trigger requires configuration to be sensitive to hadronic photoproduction reactions and at the same time reject unwanted background events. This is achieved using Field Programmable Gate Arrays (FPGAs) which allows to split the trigger into two levels: At first level all detectors with a fast read out system (up to 250 ns) are checked for hits. At the second level the number of detected particles in the Crystal Barrel is determined using the Fast Cluster Encoder (FACE), which can take up to 10 μs [Fle01]. It is always demanded that at least two particles are measured in either forward, MiniTAPS or Crystal Barrel detector while no veto from the Čerenkov detector is measured. Any information from the Crystal Barrel is only available in the second level because of the slow readout.

2.5 Software and Monte Carlo

In order to proceed with the offline data analysis of CBELSA/TAPS, several software tools are used that are described briefly in the following.

2.5.1 ExPLORA

Within the CBELSA/TAPS collaboration an analysis software has been developed named *Extended Pluggable Object-oriented Root Analysis (ExPLORA)* [Sch+]. It is based on *ROOT* [BR97] and is used for reconstruction and analysis of acquired raw data. *ROOT* has been developed at CERN to deal with a high amount of data. It makes use of *C++* libraries that give it high funcitonality regarding statistical analyses, visualizations and data management. *ExPLORA* is also written in *C++* but is operated by the use of *xml* files. This allows user specific extensions in the form of plugins that manage e.g. the application of cuts and the filling of histograms. In order to select candidates for the reaction $\gamma p \rightarrow p\eta' \rightarrow p\gamma\gamma$ a *C++* plugin has been written that was embedded into a *xml* file which managed the application of calibrations and reconstruction. For further anaylsis of the selected data, scripts in *ROOT* and *python* have been written. In appendix **??** an example `.xml` file is displayed.

2.5.2 Monte Carlo

In order to determine detector and analysis acceptances as well as possible background contributions it is convenient to simulate the according detector geometry and the interaction of particles with the material using the Monte Carlo technique [MU49]. Based on the CERN-developed software package *Geant3* (Geometry and Tracking) [Bru+87] a simulation of the CBELSA/TAPS experiment was developed using the Virtual Monte Carlo technique [Kal11]. Hereby the particles' interaction with the detector materials are modeled according to existing experimental data. Simulated datasets may then be analyzed in the same way as measured data in order to check consistency with the measured data as well as investigating detection efficiencies and background contributions. Table 3.2 shows the simulated datasets that were used during the analysis and how many events were generated for each reaction, respectively. The reactions $\gamma p \rightarrow p2\pi^0 \rightarrow p4\gamma$ $\gamma p \rightarrow p\pi^0\eta \rightarrow p4\gamma$ proved to be responsible for background contamination after the event selection (see Chapter 3). These reactions were simulated while additionally weighting all events according to the production cross section determined from a BnGa fit [AKN+; Ani+12]. These Monte Carlos were kindly provided by P. MAHLBERG [Mah22].

Reaction	Number of events
$\gamma p \rightarrow p\pi^0$	$60 \cdot 10^6$
$\gamma p \rightarrow p\eta$	$30 \cdot 10^6$
$\gamma p \rightarrow p\omega \rightarrow p\pi^0\gamma$	$30 \cdot 10^6$
$\gamma p \rightarrow p\eta' \rightarrow p\gamma\gamma$	$30 \cdot 10^6$
$\gamma p \rightarrow p2\pi^0$	$60 \cdot 10^6$
$\gamma p \rightarrow p\pi^0\eta$	$60 \cdot 10^6$
$\gamma p \rightarrow p3\pi^0$	$30 \cdot 10^6$
$\gamma p \rightarrow p2\pi^0\eta$	$30 \cdot 10^6$
$\gamma p \rightarrow n\pi^+$	$30 \cdot 10^6$
$\gamma p \rightarrow p\pi^+\pi^-$	$30 \cdot 10^6$

2.5.3 Stan

All Bayesian fits that are presented in this thesis are performed using the progamming language *Stan* [Sta22]. *Stan* is highly functional for statistical modeling and high-performance statistical computation. Full Bayesian statistical inferences can be made with MCMC sampling as well as approximate Bayesian inference with variational inference and penalized maximum likelihood estimation with optimization [Sta22]. Stan is written in *C++* and can thus handle a large amount of data very efficiently. Interfaces for different data analysis languages are available. In this thesis, the *Python* [RP22] front-end of *Stan*, called *CmdStanPy* was used. Hereby, the model is specified in a `.stan` file which is read and compiled from *Python*. All sampling statements and results can then be accessed directly from *Python*, e.g. using the package `pandas` [McK10]. Appendix **??** shows an example of a `.stan` file that can be used for the simple example of a linear fit.

2.6 Datasets

The data that was analyzed in the course of this thesis was taken in the period of July 2013 to October 2013. Unpolarized electrons from ELSA were incident on a diamond radiator with 500 µm thickness with a beam energy of $E_0 = 3.2\,\mathrm{GeV}$ and a beam current of roughly 1 nA. Thus, linearly polarized photons were created that impinged on a liquid hydrogen target. All beam times used the *vme_trig42c* that has been described previously.

The coherent edge position was chosen at 1750 MeV for the July and August beam times and at 1850 MeV for the September and October beam times, enabling an analysis of the beam asymmetry Σ in the beam energy range from $E_\gamma \approx 1100\,\mathrm{MeV}$ to 1800 MeV. 4919 runs were taken in total with alternating radiator orientation $\alpha^{\parallel/\perp} = 45°$, see Figure 4.1. The photon beam polarization was determined as part of the work [Afz19] using ANB calculations, as described in Section 2.1. Table **??** shows a summary of the key parameters of the 2013 beam time taken at the CBELSA/TAPS experiment.

beamtime	number of runs (h)	coherent edge position
July 2013	513 (111)	1750 MeV
August 2013	1832 (396)	1750 MeV
September 2013	1490 (323)	1850 MeV
October 2013	1084 (235)	1850 MeV

Table 2.1: Summary of the key parameters of the 2013 beam time at CBELSA/TAPS taken for the measurement of the beam asymmetry Σ. Taken from [Afz19].

APPENDIX A

Illustration of used software tools

A.1 ExPLORA

Figure A.1 shows an example of a `.xml` file that was used to call the plugin that was written to select the reaction $\gamma p \rightarrow p\eta' \rightarrow p\gamma\gamma$. First of all, several files have to be included in order to acquire certain *containers* that inhibit the raw data of the final state particles. Then the plugin is embedded with the options

- `MC` (bool) – determines whether Monte Carlo or measured data are analyzed
- `PWA` (bool) – determines whether used Monte Carlo simulation have PWA weights
- `FOURGAMMAS` (bool) – determines whether the generated final state has four photons or two
- `REALGAMMAS` (bool) – determines whether real photons are part of the decay or not (e.g. $n\pi^+$)
- `allroutes` (CBTConfigString) – gives the container that contains the routes of charged particles

```
1  <explora>
2      <!-- Flags can be set and later on used (e.g. as conditions) -->
3      <CBTFlag name="CONFIGS" value="/hadron/krause/git/exploraConfigs"/>
4      <CBTIncludeXML file="${CONFIGS}/Analyse/DataSource/RawData_Prefiltered.xml"/>
5      <!-- Merges particles from different sources in a common container -->
6      <CBTParticleMerger source="CBGammas,MiniTapsGammas" container="allgammas" persistent="no" />
7  
8      <!-- = Selection plugins ======================================================================= -->
9      <!-- Now you have all the particle containers and can start to select events. The analysis of preselected data starts here... -->
10     <CBTIncludeXML file="${CONFIGS}/ReactionSelection/Proton23PED.xml" />
11     <!--This is for 2.5PED events -->
12     <CBTRouteGammaFactory srccontainer="chapiroutes" dstcontainer="chapiroutegammas"/>
13     <CBTRouteGammaFactory srccontainer="FWPlugVetoRoutes" dstcontainer="fproutegammas"/>
14     <CBTRouteGammaFactory srccontainer="MiniTapsVetoRoutes" dstcontainer="minitapsroutegammas"/>
15     <CBTParticleMerger source="chapiroutegammas, fproutegammas, minitapsroutegammas" container="allroutes"/>
16     <!-- = Histogramming ============================================================================ -->
17     <!-- The histogrammer creates and fills all the histogramms which should be stored in your output file -->
18     <CBTHistogrammer profile="yes" profilehisto="yes">
19         <!--here the written plugin is called -->
20         <CBTetaprimeanalysis MC="FALSE" PWA="FALSE" FOURGAMMAS="FALSE" REALGAMMAS="TRUE" allroutes="allroutes"/>
21     </CBTHistogrammer>
22 </explora>
```

Figure A.1: Example `.xml` file that was used to call the plugin `CBTetaprimeanalysis.cpp` (line 20) with several self defined options.

A.2 Stan

The simplest regression that can be made with *Stan* is of the form

$$y = a \cdot x + b + \epsilon. \tag{A.1}$$

Here y is a measured quantity with Gaussian noise ϵ, x are predictors and a and b are slope and intercept of a linear regression. Assuming each datapoint y_n is independent and exhibits an individual noise term $\epsilon_n \sim \mathcal{N}(0, \sigma_n)$, the likelihood $p(y|a, b)$ can be formulated as

$$y_n \sim \mathcal{N}(a \cdot x_n + b, \sigma_n) \qquad \Leftrightarrow \qquad p(y|a, b) = \prod_{i=1}^{N} \mathcal{N}(y_n|a \cdot x + b, \sigma_n), \tag{A.2}$$

if there are N datapoints in total. Specifying e.g. normal priors for the two regression coefficients a and b completes the inference

$$a \sim \mathcal{N}(0, 1) \qquad\qquad b \sim \mathcal{N}(0, 1). \tag{A.3}$$

Figure A.2 shows the implementation of the described model in *Stan*. First of all, all data that is read in has to be defined. Conveniently this can be done using the `vector` class, that corresponds to a list of e.g. all x values. Next, the parameters of the model are defined and lastly the likelihood and priors are specified.

```
data {
    int<lower=0> n; //number of datapoints
    vector[n] x; //predictors
    vector[n] y; //measured quantity
    vector[n] y_Err; //measurement error
}
parameters {
    real a;
    real b;
}
model {
    //likelihood
    y ~ normal(a*x+b, y_err);
    //priors
    a ~ normal(0,1);
    b ~ normal(0,1);
}
```

Figure A.2: Example `.stan` file that can be used to perform a simple linear fit.

APPENDIX B

Additional plots and calculations

This chapter will give additional calculations and plots which would have interrupted the train of thought unnecessarily in the main part.

B.1 Statistical error for the asymmetry $A(\phi)$

Let $\tilde{N}_i^{\parallel/\perp}$ be the normalized event yields at bin ϕ_i. As mentioned in section 4.1, the asymmetry A_i at bin i is then given by

$$A_i = \frac{\tilde{N}_i^{\perp} - \tilde{N}_i^{\parallel}}{p_\gamma^{\parallel}\tilde{N}_i^{\perp} + p_\gamma^{\perp}\tilde{N}_i^{\parallel}} = \Sigma \cos\left(2\left(\alpha^{\parallel} - \phi_i\right)\right), \tag{B.1}$$

where the event yields are normalized over all M ϕ-bins

$$\tilde{N}_i^{\parallel/\perp} = \frac{N_i^{\parallel/\perp}}{\sum_{j=1}^{M} N_j^{\parallel/\perp}}.$$

To estimate statistical errors according to Gaussian error propagation, the partial derivatives with respect to $\tilde{N}_i^{\parallel/\perp}$ have to be built:

$$\left(\Delta A_i\right)^2 = \left(\frac{\partial A_i}{\partial \tilde{N}_i^{\parallel}}\Delta\tilde{N}_i^{\parallel}\right)^2 + \left(\frac{\partial A_i}{\partial \tilde{N}_i^{\perp}}\Delta\tilde{N}_i^{\perp}\right)^2, \tag{B.2}$$

where

$$\left(\frac{\partial A_i}{\partial \tilde{N}_i^{\parallel/\perp}}\right)^2 = \left[\frac{\tilde{N}_i^{\perp/\parallel}\left(p_\gamma^{\perp} + p_\gamma^{\parallel}\right)}{\left(p_\gamma^{\parallel}\tilde{N}_i^{\perp} + p_\gamma^{\perp}\tilde{N}_i^{\parallel}\right)^2}\right]^2, \tag{B.3}$$

$$\text{and with } \tilde{N}_i^{\perp/\parallel} = \tilde{N}_i \tag{B.4}$$

$$\left(\Delta\tilde{N}_i\right)^2 = \left[\frac{\partial}{\partial N_i}\left(\frac{N_i}{\sum_j N_j}\right)\cdot\Delta N_i\right]^2 + \sum_{j\neq i}\left[\frac{\partial}{\partial N_j}\left(\frac{N_i}{\sum_j N_j}\right)\cdot\Delta N_j\right]^2 \tag{B.5}$$

$$= \left[\frac{\sum_{j\neq i} N_j}{\left(\sum_j N_j\right)^2} \cdot \Delta N_i\right]^2 + \sum_{j\neq i}\left[-1 \cdot \frac{N_i}{\left(\sum_j N_j\right)^2} \cdot \Delta N_j\right]^2 \tag{B.6}$$

$$= \frac{1}{\left(\sum_j N_j\right)^4} \cdot \left[\left(\sum_{j\neq i} N_j \cdot \Delta N_i\right)^2 + \sum_{j\neq i}\left(N_i \cdot \Delta N_j\right)^2\right]. \tag{B.7}$$

One can then further use that $\left(\Delta N_i\right)^2 \approx N_i$. This holds only approximately, since the histograms are filled N times with weights w_n (see chapter 3.3), but since the weights are either $w = 1$ or $w \ll 1$

$$\Delta N_i = \sqrt{\sum_{n=1}^{N} w^2} \approx \sqrt{N_i}. \tag{B.8}$$

B.2 Kinematic variables for each bin

B.2.1 Coplanarity

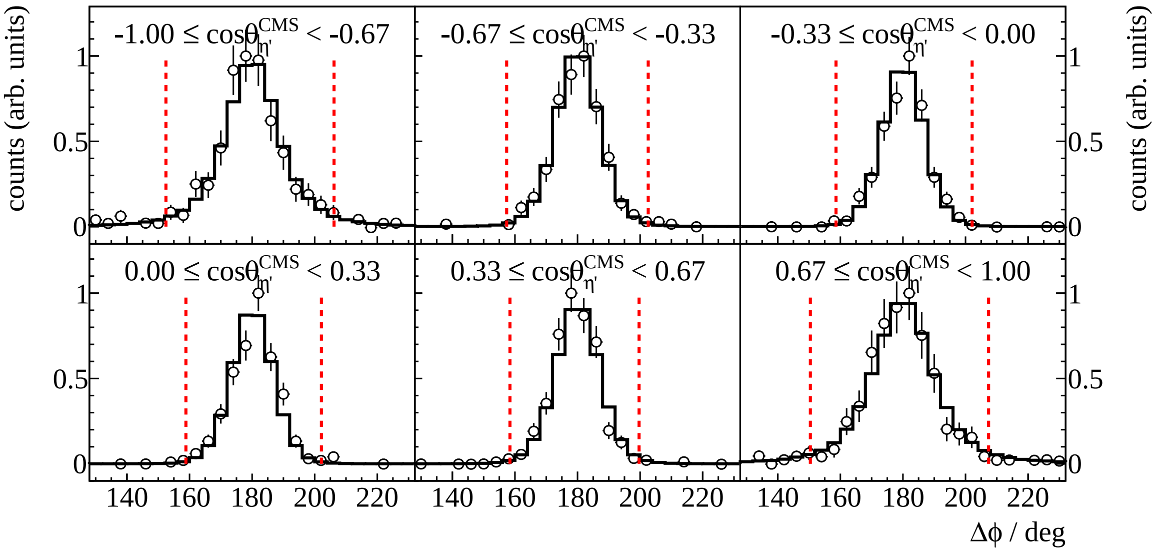

(a) 1500 MeV ≤ E_γ < 1600 MeV

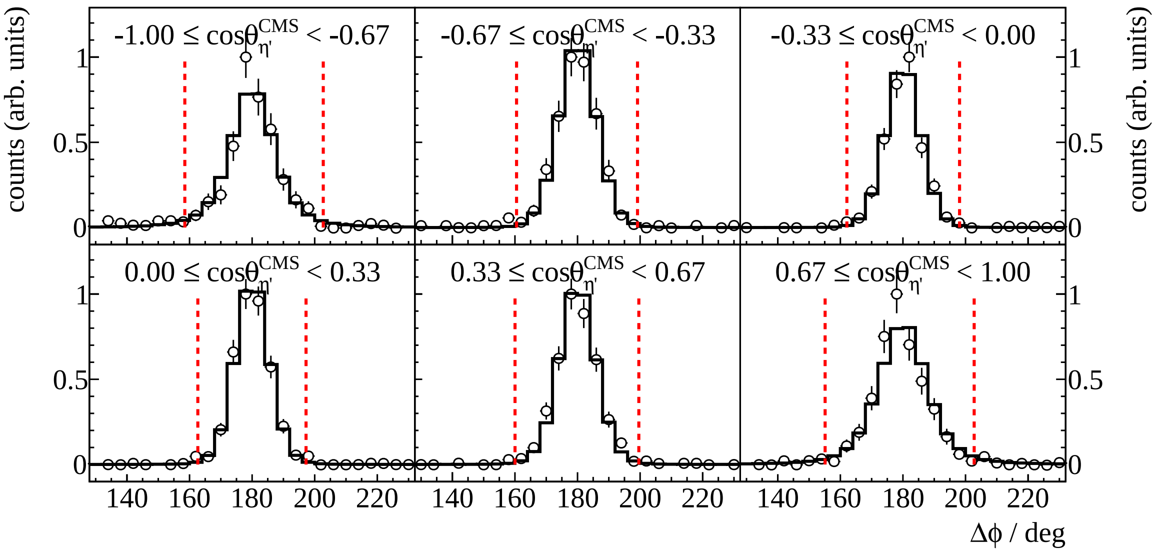

(b) 1600 MeV ≤ E_γ < 1700 MeV

Figure B.1: Coplanarity $\Delta\phi$ for all energy and angular bins. Data points are displayed as open circles, scaled Monte Carlo data belonging to η' photoproduction is displayed as solid histogram. The determined cut ranges are indicated by the dashed red lines.

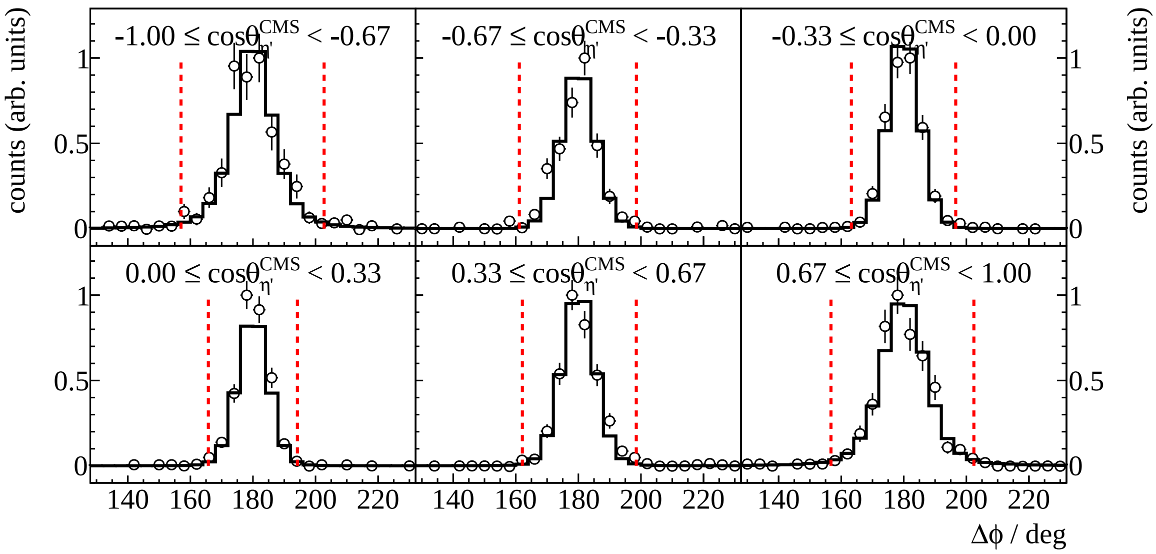

(c) 1700 MeV ≤ E_γ < 1800 MeV

Figure B.1: Coplanarity $\Delta\phi$ for all energy and angular bins. Data points are displayed as open circles, scaled Monte Carlo data belonging to η' photoproduction is displayed as solid histogram. The determined cut ranges are indicated by the dashed red lines.

Figure B.1 shows the coplanarity for all energy and angular bins. Cut ranges were determined from a Gaussian fit to the data points. Only slight dependency on beam energy and meson polar angle can be identified. Only η' Monte Carlo data are fitted because the measured points do not give enough reference points for the fit to identify different contributing final states. There is good agreement between Monte Carlo simulations and measured data.

B.2.2 Polar angle difference

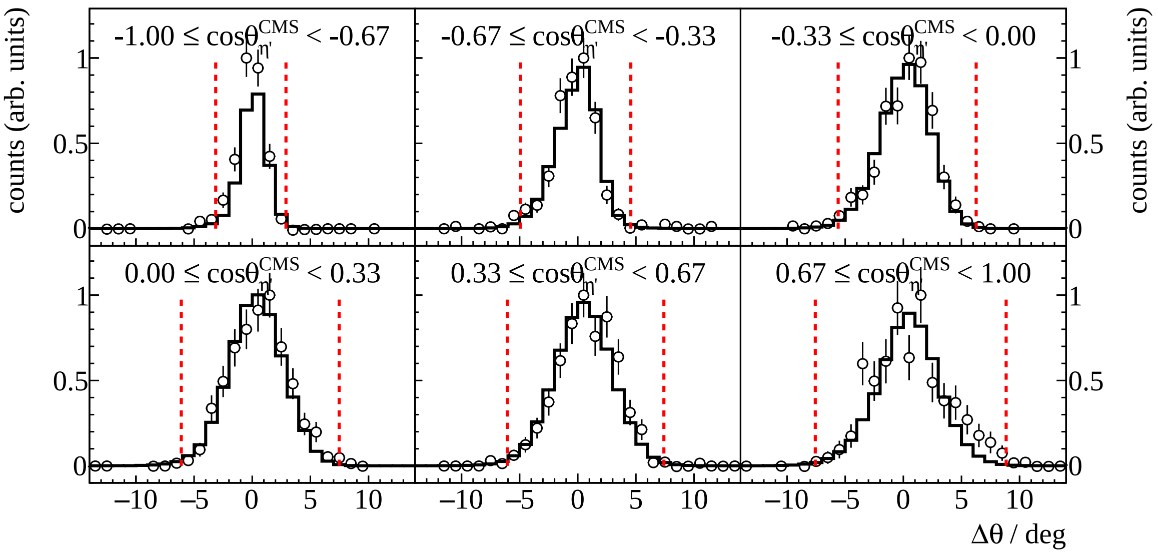

(a) 1500 MeV ≤ E_γ < 1600 MeV

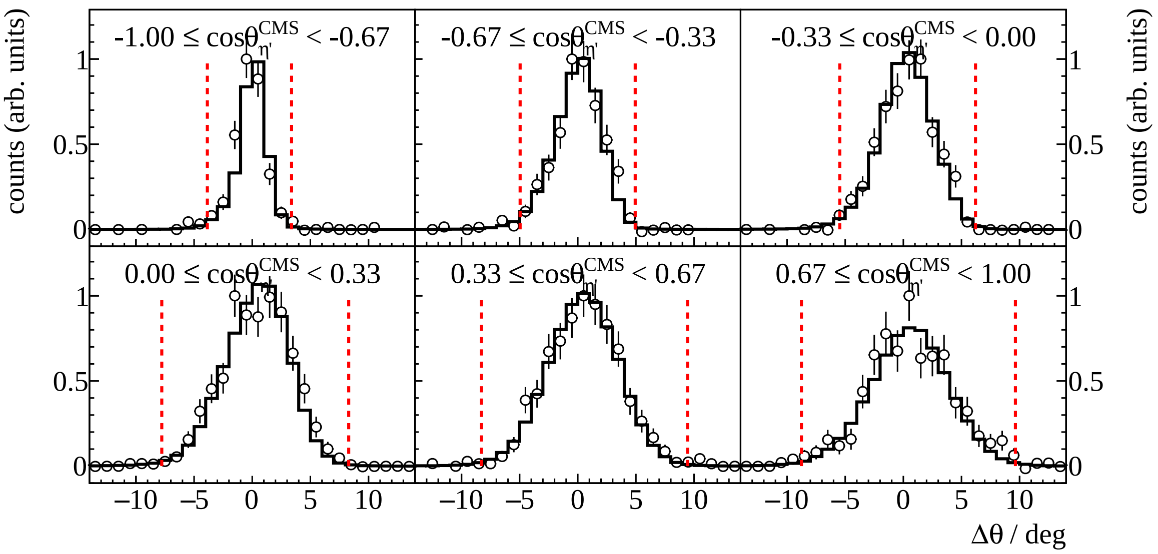

(b) 1600 MeV ≤ E_γ < 1700 MeV

Figure B.2: Polar angle difference $\Delta\theta$ for all energy and angular bins. Data points are displayed as open circles, scaled Monte Carlo data belonging to η' photoproduction is displayed as solid histogram. The determined cut ranges are indicated by the dashed red lines.

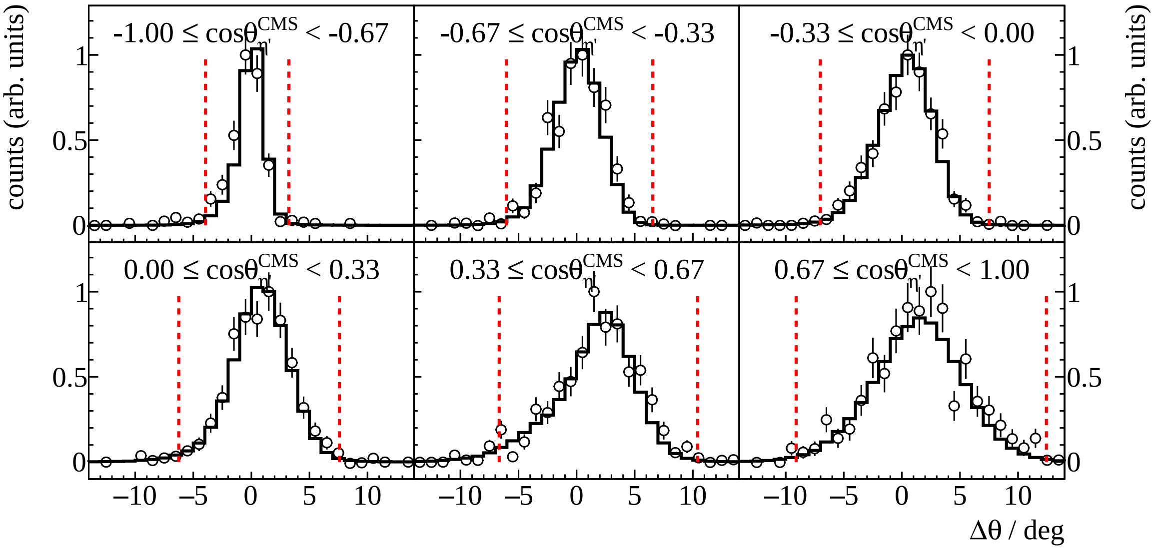

(c) 1700 MeV ≤ E_γ < 1800 MeV

Figure B.2: Polar angle difference $\Delta\theta$ for all energy and angular bins. Data points are displayed as open circles, scaled Monte Carlo data belonging to η' photoproduction is displayed as solid histogram. The determined cut ranges are indicated by the dashed red lines.

Figure B.2 shows the polar angle difference for all energy and angular bins. Cut ranges were determined from a Gaussian fit to the data points. Only slight dependency on beam energy can be identified whereas clear correlation between width of the distribution and meson polar angle exists. This is due to the hit detectors which exhibit different angular resolutions, as has been discussed in the main part. Only η' Monte Carlo data are fitted because the measured points do not give enough reference points for the fit to identify different contributing final states. There is good agreement between Monte Carlo simulations and measured data.

B.2.3 Missing mass

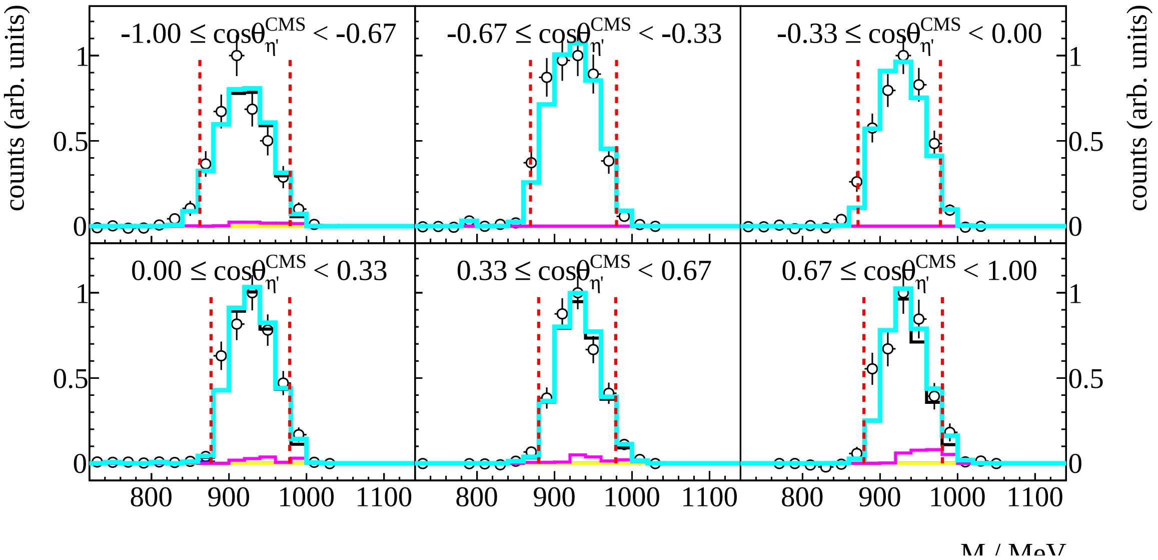

(a) 1500 MeV ≤ E_γ < 1600 MeV

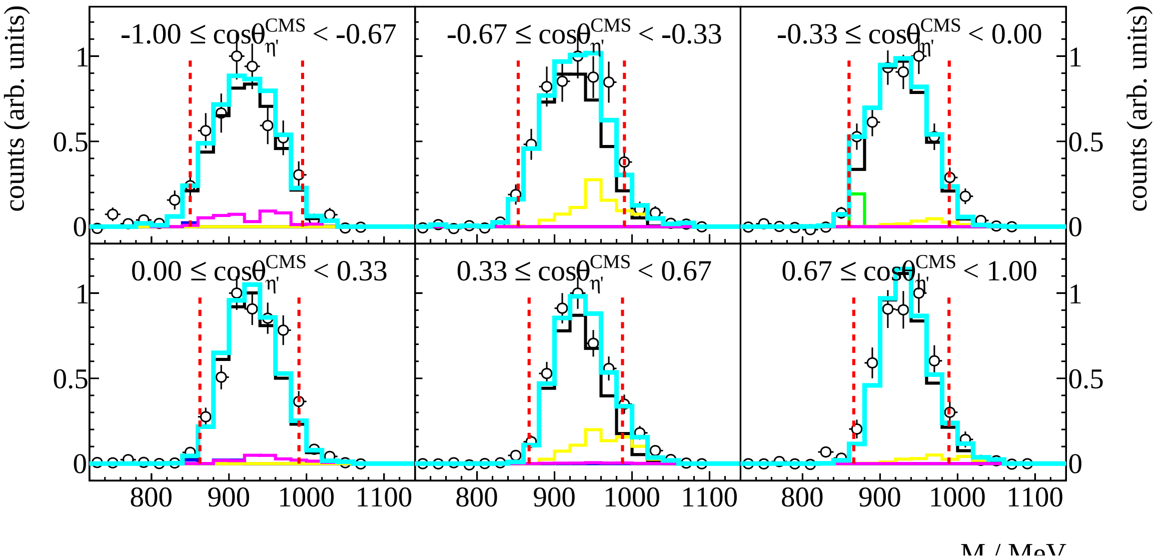

(b) 1600 MeV ≤ E_γ < 1700 MeV

Figure B.3: Missing mass m_x for all energy and angular bins. Data points are displayed as open circles, scaled Monte Carlo data belonging to η' (black), $2\pi^0$ (yellow) and $\pi^0\eta$ (magenta) photoproduction is displayed as solid histogram while their sum is displayed as turquoise histogram. The determined cut ranges are indicated by the dashed red lines.

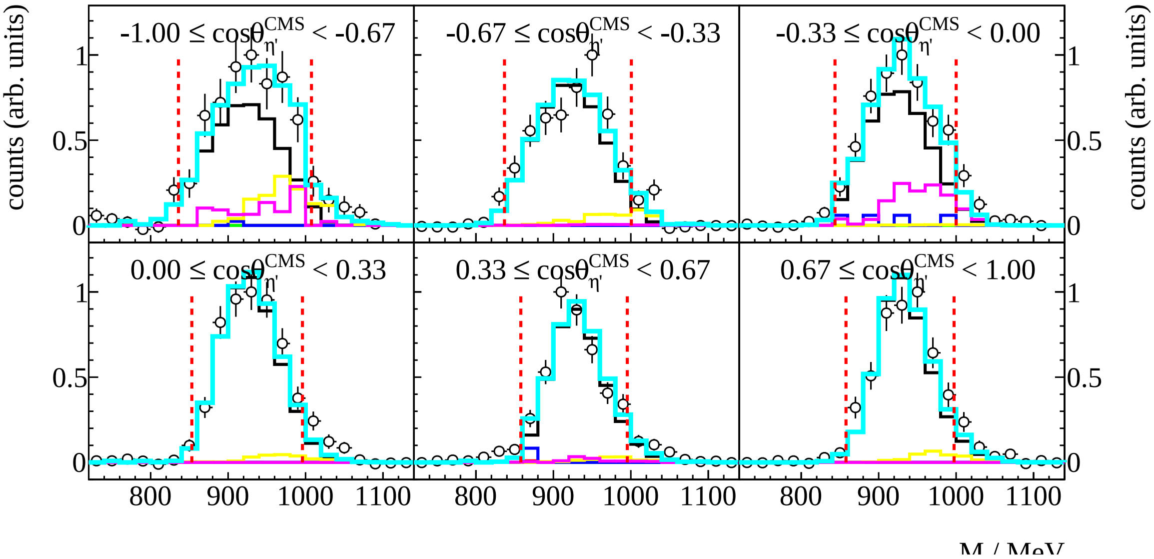

(c) 1700 MeV ≤ E_γ < 1800 MeV

Figure B.3: Missing mass m_X for all energy and angular bins. Data points are displayed as open circles, scaled Monte Carlo data belonging to η' (black), $2\pi^0$ (yellow) and $\pi^0\eta$ (magenta) photoproduction is displayed as solid histogram while their sum is displayed as turquoise histogram. The determined cut ranges are indicated by the dashed red lines.

Figure B.3 shows the missing mass for all energy and angular bins. Cut ranges were determined from a Novosibirsk fit to the Monte Carlo data. Only slight dependency on meson polar angle can be identified. Especially at higher beam energies the missing mass peak grows wider with flat background contributions from $2\pi^0$ and $\pi^0\eta$ production towards higher masses. The Monte Carlo fit mostly shows consistency with the fit of the invariant mass spectra. However, spectra are to be seen with caution, since the shapes of the two different background contributions are very similar and there is no other reference point in the missing mass spectrum as opposed to the invariant mass. Fits to the invariant mass spectra may reveal background contributions where a fit to the missing mass spectrum failed to find any. There is good agreement between Monte Carlo simulations and measured data.

B.2.4 Invariant mass

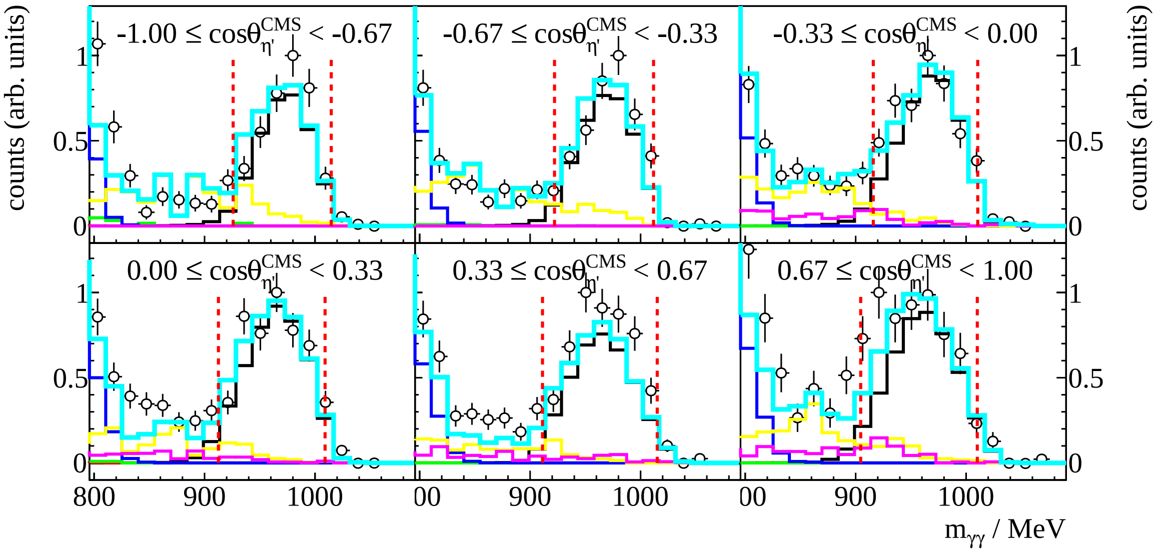

(a) 1500 MeV ≤ E_γ < 1600 MeV

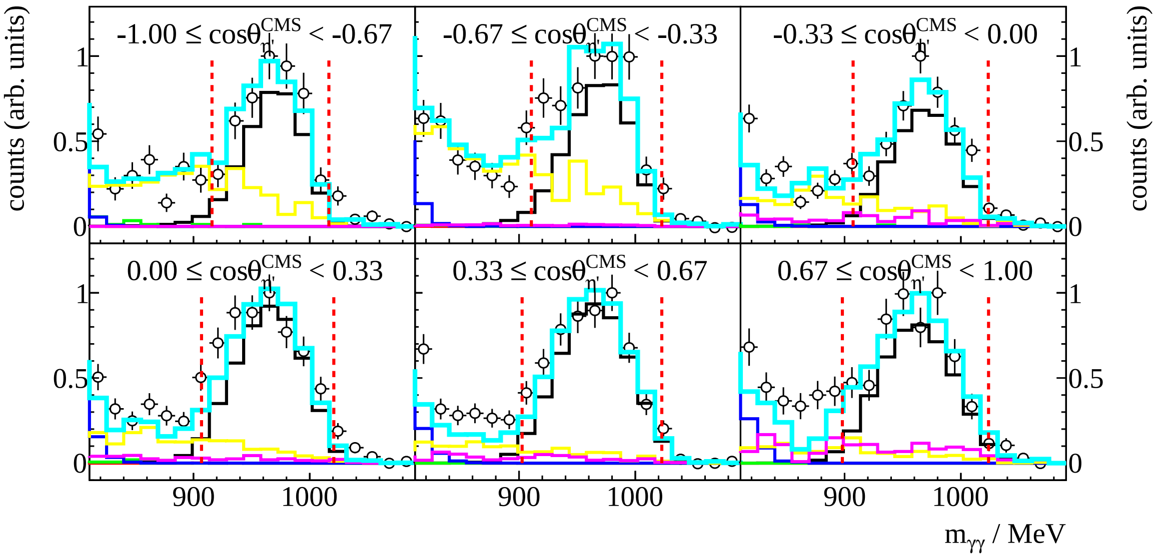

(b) 1600 MeV ≤ E_γ < 1700 MeV

Figure B.4: Invariant mass m_{meson} for all energy and angular bins. Data points are displayed as open circles, scaled Monte Carlo data belonging to η' (black), $2\pi^0$ (yellow), $\pi^0\eta$ (magenta), π^0 (green) and ω (blue) photoproduction is displayed as solid histogram while their sum is displayed as turquoise histogram. The determined cut ranges are indicated by the dashed red lines.

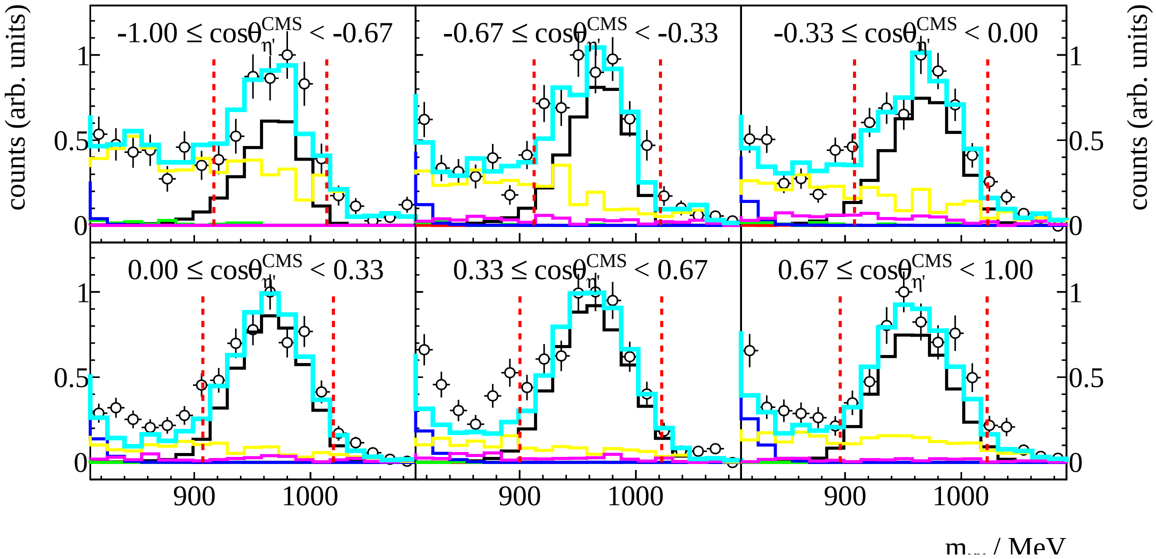

(c) 1700 MeV $\leq E_\gamma <$ 1800 MeV

Figure B.4: Invariant mass m_{meson} for all energy and angular bins. Data points are displayed as open circles, scaled Monte Carlo data belonging to η' (black), $2\pi^0$ (yellow), $\pi^0\eta$ (magenta), π^0 (green) and ω (blue) photoproduction is displayed as solid histogram while their sum is displayed as turquoise histogram. The determined cut ranges are indicated by the dashed red lines.

Figure B.4 shows the invariant mass for all kinematic bins. Hardly any dependence on meson direction and beam energy is observed. However, background contributions are especially observed in very forward and backward direction towards higher beam energies in consistency with findings from the missing mass spectra. A flat background is realized by $2\pi^0$ and $\pi^0\eta$ production. There is good agreement between Monte Carlo simulations and measured data.

APPENDIX C

Discussion of binned fits

Investigation of toy Monte Carlo experiments (cf. section 4.3) revealed that the choice of binning leads to systematic errors regarding the parameter Σ when fitting a binned distribution to the equation

$$A(\phi) = \Sigma \cdot \cos\left(2\left(\alpha^{\parallel} - \phi\right)\right). \tag{C.1}$$

To investigate this further, the distributions $A(\phi)$ from different toy Monte Carlo experiments where fitted for several binnings in ϕ. Three different Monte Carlo experiments were considered, each corresponding roughly to the expected statistics in one kinematic bin for π^0, η and η' photoproduction, respectively. For simplicity's sake, only least squares fits are shown here, although similar results were found for Bayesian fits also. The equivalency of Bayesian and least squares fit has been demonstrated sufficiently up until now. To identify the bias that is introduced by binning the data, 10000 toy Monte Carlo bins for each setting are fitted for $n = 10, 15, 20, \ldots, 100$ bins. Then the dependence from the amount of bins of the mean μ of the normalized residuals ξ as well as the mean χ^2 value of all fits is investigated. This is shown in Figure C.1; The fitted mean of the normalized posteriors ξ is plotted against the number of bins (blue data points, left ordinate) as well as the mean χ^2 of 10000 fits depending on the number of bins (red data points, right ordinate). Clear dependencies can be made out: while too few bins tend to underestimate the true value of the beam asymmetry, too much bins will lead to an overcompensation. For this reason, the functions $\chi^2(n)$ and $\mu(n)$ are monotonously rising with increasing number of bins n. An exception is realized by the samples that simulated the statistics of the η' final state, which can be explained by the fact, that after reaching a certain number of bins, no sensible fit estimates can be made anymore because too few data points are available. A minimum deviation from the nominal value is reached with $n = 10, 20, 30$ bins for statistics comparable to η', η and π^0 production respectively. This does not coincide with a minimum χ^2 necessarily, although the mean χ^2 values associated with the best estimation of the input value are compatible with 1. Figure C.1 however remarkably shows the influence binning has on the extraction of the beam asymmetry. Since there exist other methods, binned fits should only be used as a sanity check, but generally avoided, to circumvent the introduction of any systematics inherent to binning.

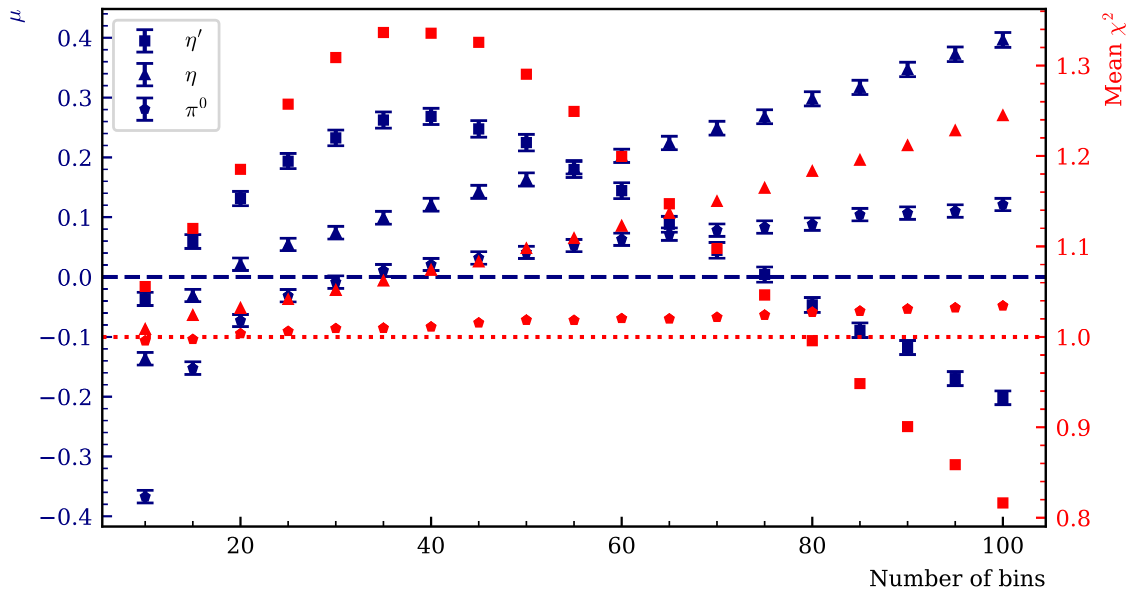

Figure C.1: Fit performance in dependence of the number of bins. Left axis shows the mean μ of the distribution of the normalized residuals ξ, right axis shows the mean χ^2 of all fits. Squares simulate fits with statistics similar to the $\gamma p \to p\eta' \to p\gamma\gamma$ final state, triangles statistics similar to the $\gamma p \to p\eta \to p\gamma\gamma$ and final state, pentagons statistics similar to the $\gamma p \to p\pi^0 \to p\gamma\gamma$. Dotted red line indicates the ideal value of $\chi^2 = 1$, while the dashed blue line indicates the ideal mean of the normalized residuals at $\mu = 0$.

APPENDIX D

Investigation of posteriors without truncation

In section 4.3 the investigation of posterior distributions from unbinned Bayesian fits was incomplete, since the normalized residuals as well as the likelihood pool could not be built with truncated posteriors. This is now supplemented here. After the fits have been repeated without implementing a truncation for the posteriors, all introduced measures to argue good fit quality can be examined. As a reminder, the data were generated with $\Sigma_1 = 0.5$ and $\Sigma_t = -0.5$. Figure D.1 shows the combined posteriors of all fits. The left hand side shows the normalized residuals Ξ and the right hand side the unnormalized combination of all posteriors. The results completely meet the expectations, the input values for the beam asymmetries are very well reproduced, and the normalized residuals follow a standard normal distribution as Gaussian fits show. Together with the results obtained from the independent likelihood pool (Figure D.2), which is able to reproduce the input values within 1σ, this suffices to conclude correct estimation of distribution widths with no inherent bias, as had already been found in section 4.2.3.

Remark: It turned out that without the amount of statistics that was used in section 4.2, normal priors centered at 0 for the asymmetries Σ_t and Σ will mislead the fit results for these parameters towards 0 if no lower and upper boundaries are used. Instead the priors were then chosen to be uniform on the interval $[-2, 2]$. This imposes boundaries, but will not truncate the posteriors because the distributions are not expected to be this wide. All distributions shown here are generated using this model to complete the full investigation of posteriors. Previous toy Monte Carlo experiments (Figure 4.19) as well as very good agreement between point estimates and posterior distributions (Figure 4.23) together with the results shown here confirm the validity of the fit used in the main part.

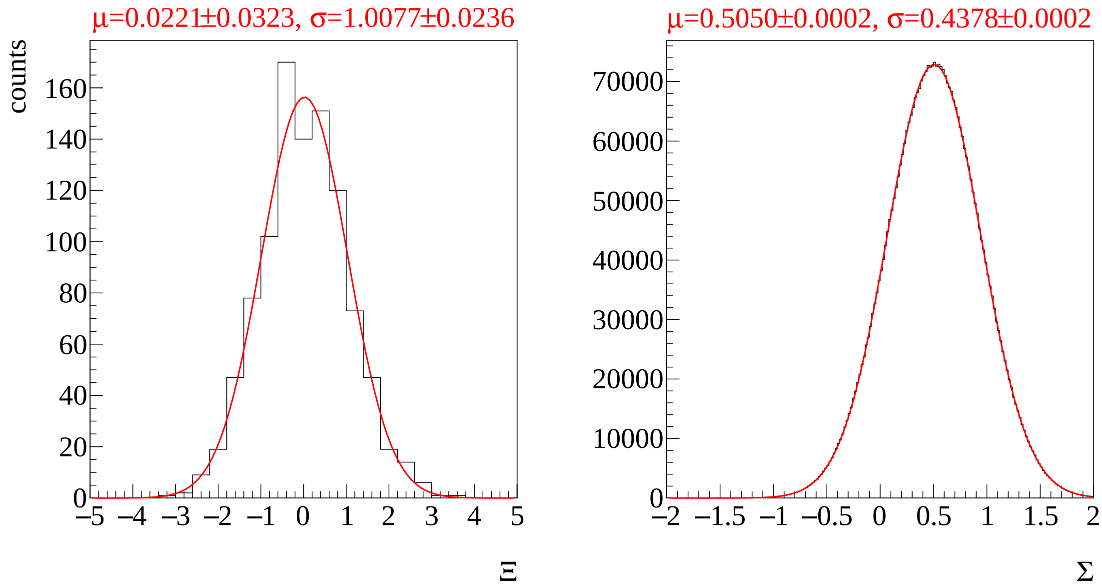

(a) Beam asymmetry Σ_1

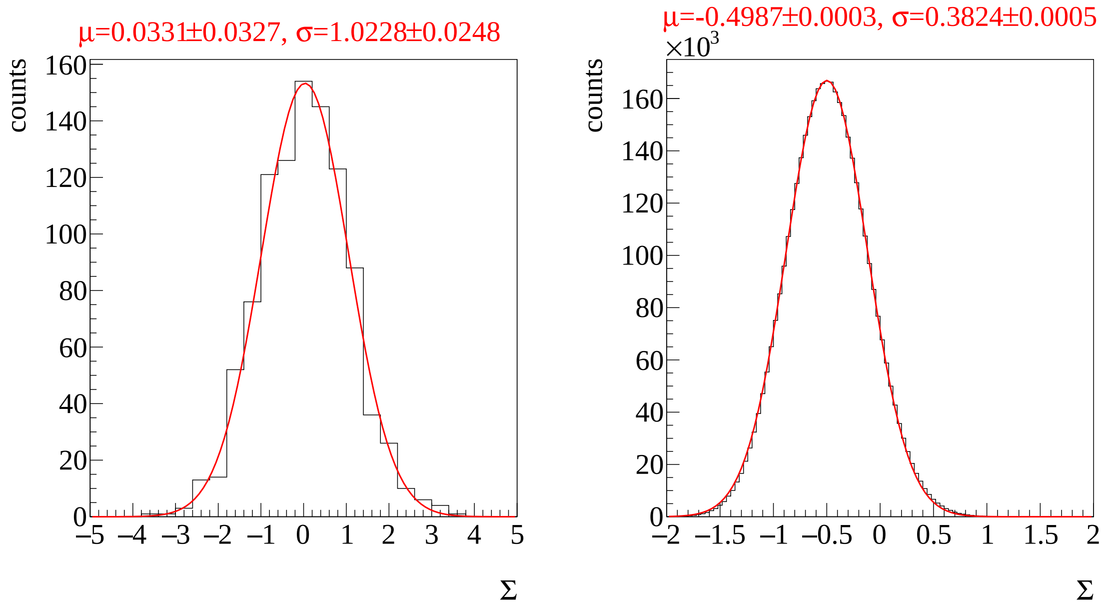

(b) Background beam asymmetry Σ_t

Figure D.1: Combined posteriors of all 1000 fits without truncation for the signal beam asymmetry Σ_1 and the background beam asymmetry Σ_t. Left: normalized residuals Ξ, Right: unaltered added posterior distributions. Gaussian fits have been performed with results given on top of each plot.

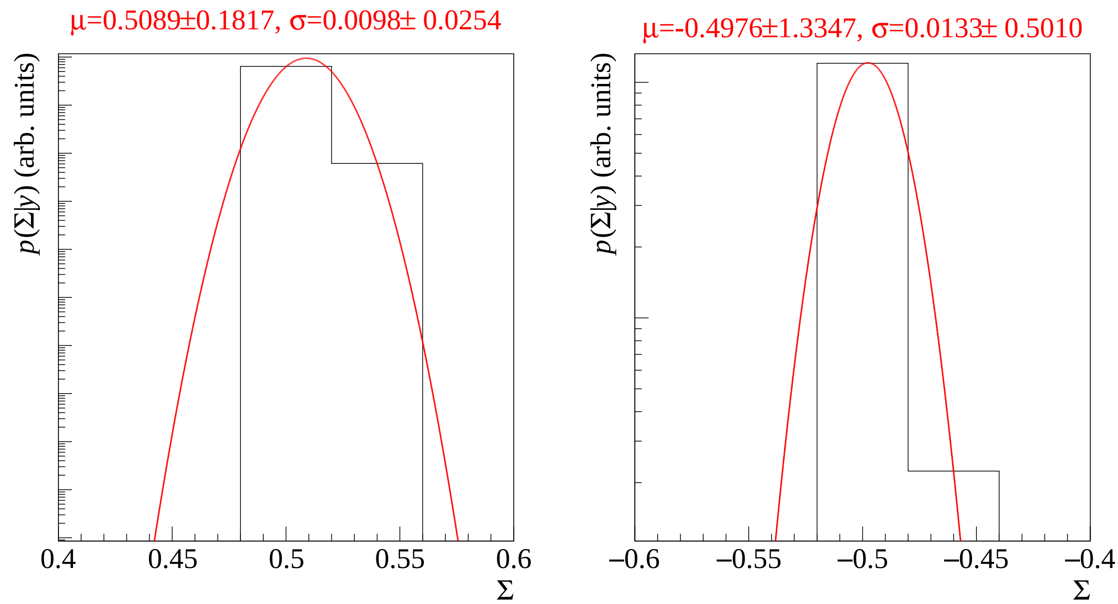

Figure D.2: Posterior distributions of Σ_1 (left) and Σ_t (right) combined in an independent likelihood pool. Gaussian fits to the distribution confirm the reproduction of the input values within 1σ. Note that only very few datapoints were available for the fits, because the distributions overwhelmingly converge into a single bin at ±0.5, hence the large errors on the fit parameters.

Bibliography

[Afz19] F. N. Afzal, *Measurement of the beam and helicity asymmetries in the reactions $\gamma p \rightarrow p\pi^0$ and $\gamma p \rightarrow p\eta$*,
PhD thesis: Rheinische Friedrich-Wilhelms-Universität Bonn, 2019,
URL: https://hdl.handle.net/20.500.11811/8064
(cit. on pp. 7, 9, 11, 12, 15, 17).

[Leo94] W. R. Leo,
Techniques for Nuclear and Particle Physics Experiments, A How-to Approach, vol. 2,
Springer-Verlag Berlin Heidelberg GmbH, 1994 (cit. on pp. 8, 13, 14).

[Hei54] W. Heithler, *The Quantum Theory of Radiation*, Oxford University Press, 1954
(cit. on p. 8).

[Dem10] W. Demtröder, *Experimentalphysik 3, Atome, Moleküle, Festkörper*, vol. 4,
Springer-Verlag Berlin Heidelberg New York, 2010 (cit. on p. 8).

[Nat+03] F. Natter, P. Grabmayr, T. Hehl, R. Owens and S. Wunderlich, *Monte Carlo simulation and analytical calculation of coherent bremsstrahlung and its polarisation*,
Nuclear Instruments and Methods in Physics Research Section B: Beam Interactions with Materials and Atoms **211** (2003) 465 (cit. on p. 9).

[Els+09] D. Elsner et al., *Linearly polarised photon beams at ELSA and measurement of the beam asymmetry in π^0 photoproduction off the proton*,
The European Physical Journal A **39** (2009) 373,
URL: https://doi.org/10.1140%2Fepja%2Fi2008-10708-1 (cit. on p. 9).

[Kam10] S. Kammer, *Strahlpolarimetrie am CBELSA/TAPS Experiment*,
PhD thesis: Rheinische Friedrich-Wilhelms-Universität Bonn, 2010,
URL: https://hdl.handle.net/20.500.11811/4539 (cit. on p. 9).

[For10] K. Fornet-Ponse,
Die Photonenmarkierungsanlage für das Crystal-Barrel/TAPS-Experiment an ELSA,
PhD thesis: Rheinische Friedrich-Wilhelms-Universität Bonn, 2010,
URL: https://hdl.handle.net/20.500.11811/4507 (cit. on p. 10).

[Har08] J. Hartmann, *Zeitkalibrierung und Photonenflussbestimmung für das Crystal-Barrel-Experiment and ELSA*,
Diploma thesis: Rheinische Friedrich-Wilhelms-Universität Bonn, 2008
(cit. on pp. 10, 11, 13–15).

[Wal] D. Walther, *Crystal Barrel, A 4π photon spectrometer*,
URL: https://www.cb.uni-bonn.de (visited on 27/09/2021) (cit. on pp. 10, 14).

[Ham09] C. Hammann, *Aufbau eines Flüssigwasserstofftargets zur Durchführung von Kalibrationsmessungen am Crystal-Barrel Experiment an ELSA*, Diploma thesis: Rheinische Friedrich-Wilhelms-Universität Bonn, 2009 (cit. on pp. 10, 11).

[Fös00] A. Fösel, *Entwicklung und Bau des Innendetektors für das Crystal Barrel Experiment an ELSA/Bonn*, PhD thesis: Friedrich-Alexander-Universität Erlangen-Nürnberg, 2000 (cit. on p. 11).

[Suf+05] G. Suft et al., *A scintillating fibre detector for the Crystal Barrel experiment at ELSA*, Nucl. Instrum. Meth. A **538** (2005) 416 (cit. on p. 11).

[PDG] PDG, *Atomic and Nuclear Properties*, URL: `https://pdg.lbl.gov/2022/AtomicNuclearProperties/index.html` (visited on 04/08/2022) (cit. on pp. 11, 13, 14).

[Ake+92] E. Aker et al., *The Crystal Barrel spectrometer at LEAR*, Nucl. Instrum. Meth. A **321** (1992) 69 (cit. on pp. 12, 13).

[Urb17] M. Urban, *Design eines neuen Lichtpulsersystems sowie Aufbau und Inbetriebnahme der neuen APD Auslese für das Crystal-Barrel-Kalorimeter*, PhD thesis: Rheinische Friedrich-Wilhelms-Universität Bonn, 2017 (cit. on pp. 12, 13).

[Jun04] J. Junkersfeld, *Kalibration des Crystal-Barrel-ELSA Detektors mit Hilfe der Reaktion* $\gamma p \rightarrow p\pi^0$, Diploma thesis: Rheinische Friedrich-Wilhelms-Universität Bonn, 2004 (cit. on p. 13).

[Bet30] H. Bethe, *Zur Theorie des Durchgangs schneller Korpuskularstrahlen durch Materie*, Annalen der Physik **397** (1930) 325, eprint: `https://onlinelibrary.wiley.com/doi/pdf/10.1002/andp.19303970303`, URL: `https://onlinelibrary.wiley.com/doi/abs/10.1002/andp.19303970303` (cit. on p. 13).

[Hon14] C. Honisch, *Design, Aufbau und Test einer neuen Ausleseelektronik für das Crystal-Barrel-Kalorimeter*, PhD thesis: Rheinische Friedrich-Wilhelms-Universität Bonn, 2014 (cit. on p. 13).

[Wen04] C. Wendel, *Entwicklung eines Szintillations-Detektors zur Identifikation geladener Teilchen im Crystal-Barrel Vorwärtsdetektor*, Diploma thesis: Rheinische Friedrich-Wilhelms-Universität Bonn, 2004 (cit. on p. 13).

[Geh15] S. Gehring, *Test des Szintillationsdetektors zur Identifikation geladener Teilchen im Crystal-Barrel-Vorwärtsdetektor*, Bachelor thesis: Rheinische Friedrich-Wilhelms-Universität Bonn, 2015 (cit. on p. 13).

[Gab+94] A. Gabler et al., *Response of TAPS to monochromatic photons with energies between 45 and 790 MeV*, Nuclear Instruments and Methods in Physics Research Section A: Accelerators, Spectrometers, Detectors and Associated Equipment **346** (1994) 168, ISSN: 0168-9002, URL: `https://www.sciencedirect.com/science/article/pii/0168900294907013` (cit. on pp. 13, 14).

[Str96] H. Ströher, *Electromagnetic and Hadronic Probes of Nuclear Matter: Portrait of the European Photon Detector TAPS*, Nuclear Physics News **6** (1996) 7, eprint: https://doi.org/10.1080/10506899609411060, URL: https://doi.org/10.1080/10506899609411060 (cit. on p. 13).

[Nov91] R. Novotny, *The BaF/sub 2/ photon spectrometer TAPS*, IEEE Transactions on Nuclear Science **38** (1991) 379 (cit. on p. 13).

[Kai07] D. Kaiser, *Aufbau und Test des Gas- Čerenkov-Detektors für den Crystal-Barrel-Aufbau an ELSA*, Diploma thesis: Rheinische Friedrich-Wilhelms-Universität Bonn, 2007 (cit. on p. 14).

[McG08] W. McGehee, *The Gamma Intensity Monitor of the Crystal-Barrel-Experiment*, Bachelor thesis: Massachusets Institute of Technology, 2008 (cit. on p. 14).

[Die08] J. Dielmann, *Entwicklung, Aufbau und Test eines Detektors zur Bestimmung des Photonenflusses an der Bonner Photonenmarkierungsanlage*, Diploma thesis: Rheinische Friedrich-Wilhelms-Universität Bonn, 2008 (cit. on p. 15).

[Win06] A. Winnebeck, *Entwicklung und Implementierung eines universellen, FPGA basierten Triggermoduls für das Crystal-Barrle-Experiment and ELSA*, Diploma thesis: Rheinische Friedrich-Wilhelms-Universität Bonn, 2006 (cit. on p. 15).

[Hof18] P. Hoffmeister, *Das Datenerfassungssystem für das Crystal-Barrel/TAPS-Exoeriment an ELSA*, PhD thesis: Rheinische Friedrich-Wilhelms-Universität Bonn, 2018 (cit. on p. 15).

[Fle01] H. Flemming, *Entwurf und Aufbau eines Zellularlogik-Triggers für das Crystal-Barrel-Experiment an der Elektronenbeschleunigeranlage ELSA*, PhD thesis: Rheinische Friedrich-Wilhelms-Universität Bonn, 2001 (cit. on p. 15).

[Sch+] C. Schmidt et al., *Extended Pluggable Object-oriented Root Analysis*, URL: https://explora.cb.uni-bonn.de (visited on 10/08/2022) (cit. on p. 16).

[BR97] R. Brun and F. Rademakers, *ROOT — An object oriented data analysis framework*, Nucl. Instrum. Meth. A **389** (1997) 81, ISSN: 0168-9002, URL: https://www.sciencedirect.com/science/article/pii/S016890029700048X (cit. on p. 16).

[MU49] N. Metropolis and S. Ulam, *The Monte Carlo Method*, Journal of the American Statistical Association **44** (1949) 335, PMID: 18139350, eprint: https://www.tandfonline.com/doi/pdf/10.1080/01621459.1949.10483310, URL: https://www.tandfonline.com/doi/abs/10.1080/01621459.1949.10483310 (cit. on p. 16).

[Bru+87] R. Brun, F. Bruyant, M. Maire, A. C. McPherson and P. Zanarini, *GEANT3*, (1987) (cit. on p. 16).

[Kal11] F. Kalischewski, *Development of a new simulation for the CBELSA/TAPS experiment using Virtual Monte Carlo*, Diploma thesis: Rheinische Friedrich-Wilhelms-Universität Bonn, 2011 (cit. on p. 16).

[AKN+] A. Anisovich, E. Klempt, V. Nikonov et al., *Bonn-Gatchina Partial Wave Analysis*, URL: https://pwa.hiskp.uni-bonn.de/ (visited on 10/08/2022) (cit. on p. 16).

[Ani+12] A. V. Anisovich et al., *Properties of baryon resonances from a multichannel partial wave analysis*, The European Physical Journal A **48** (2012), URL: https://doi.org/10.1140%2Fepja%2Fi2012-12015-8 (cit. on p. 16).

[Mah22] P. Mahlberg, *Thesis in Preparation*, Rheinische Friedrich-Wilhelms-Universität Bonn, 2022 (cit. on p. 16).

[Sta22] Stan development team, *Stan Modeling Language Users Guide and Reference Manual*, vol. 2.29, 2022, URL: https://mc-stan.org (cit. on p. 17).

[RP22] G. van Rossum and the Python development team, *The Python Language Reference, Release 3.10.5*, 2022, URL: https://docs.python.org/3.10/reference/index.html (cit. on p. 17).

[McK10] W. McKinney, "Data Structures for Statistical Computing in Python", *Proceedings of the 9th Python in Science Conference*, ed. by S. van der Walt and J. Millman, 2010 56 (cit. on p. 17).

List of Figures

List of Tables